A phenomenological explanation of the autoignition propagation under HCCI conditions

José M. Desantes[a], J. Javier López[a,*], José M. García-Oliver[a], Darío López-Pintor[a]

[a]*CMT-Motores Térmicos*
Universitat Politècnica de València
Camino de Vera, s/n. 46022 Valencia, SPAIN

Abstract

A phenomenological explanation about the autoignition propagation under HCCI conditions is developed in this paper. To do so, diffusive effects from the burned zones to the fresh mixture, pressure waves based effects and expansion effects caused by combustion are taken into account. Additionally, different Damköhler numbers have been defined and evaluated in order to characterize the phenomenon and quantify the relevance of each effect. The theoretical explanation has been evaluated by means of chemiluminescence measurements performed in a Rapid Compression Expansion Machine (RCEM), which allow to estimate the velocity of propagation of the autoignition front. The results showed that under HCCI conditions the autoignition propagation is controlled, in general, by the pressure waves established in the combustion chamber, since the characteristic time of the autoignition propagation is too short to assume the absence of pressure gradients in the chamber. Thus, the thermodynamic conditions reached behind the pressure

*Corresponding author
Tel: +34 963 879 232. Fax: +34 963 877 659. E-mail: *jolosan3@mot.upv.es*

wave promote the autoignition and explain the high propagation velocities associated to the reaction front. Besides, the results also showed that the contribution of diffusive phenomena on the propagation is negligible, since the characteristic time of diffusion is too long compared to the characteristic time of the autoignition propagation. Finally, the experimental measurements showed that the autoignition propagation is affected by a really relevant cycle-to-cycle variation. The turbulence generated by the combustion has, by definition, an aleatory behavior, leading to random heterogeneity distribution and, therefore, to somewhat random autoignition propagation.

Keywords: RCEM, chemiluminescence, autoignition propagation

1. Introduction, justification and objective

New combustion modes based on autoignition under Low Temperature Conditions (LTC), such as Homogeneous Charge Compression Ignition (HCCI), Partially Premixed Compression Ignition (PPCI) and others, have shown to be a good solution to reduce pollutant emissions while keeping, or even improving, the engine efficiency [1]. However, new combustion strategies have shown different challenges to overcome before implementing these technologies in commercial engines. On the one hand, the autoignition event is hardly controllable because of the absence of an ignition event (spark in SI-engines or injection in conventional CI-engines) [2]. On the other hand, the maximum load is limited by the extremely high pressure rise rate that occurs in autoignition events, which leads to high level of noise and unacceptable mechanical strains [3].

Sequential autoignition is an intrinsic phenomenon to these new combus-

tion modes. First, stratified charges have shown to be able to increase the operating load range in LTC CI-engines [4]. A reactivity gradient is induced by means of a direct injection process, leading to a sequential autoignition. Then, the existence of small heterogeneties caused by wall effects and heat losses under theoretically homogeneous conditions (e.g., HCCI conditions) lead to a reactivity gradient and, therefore, to a sequential autoignition [5].

Several experimental and simulation works have been performed about the thermal stratification in autoignition studies [6], and not only under HCCI conditions, but also for the study of knocking in SI-engines [7] or for the study of noise [8].

Sjöberg et al. [9] studied the role of the natural thermal stratification on the combustion duration and on the pressure rise rate experimentally in an HCCI engine and by simulation solving a multi-zone model in CHEMKIN. The authors found that natural thermal stratification generated by heat losses can explain the progressive pressure rise that is typical of this combustion mode. Furthermore, Bradley et al. [10] showed that a critical temperature gradient from which the autoignition propagation reaches acoustic conditions can be estimated, which is a concept also studied by Gu et al. [11].

Moreover, Chen et al. [12] studied the effect of thermal stratification on H_2 autoignition by means of direct numerical simulations. The authors found that autoignition propagation seems to be inversely proportional to $\bigtriangledown T$ for medium-to-low temperature gradients, while diffusive effects become relevant when $\bigtriangledown T$ increases. Besides, the ignition delay seems to be governed by the competition between accumulation of chain carriers and diffusion in

the different zones of the combustion chamber.

Finally, Yoo et al. [13] studied the sequential autoignition of n-heptane by thermal stratification using direct numerical simulations (DNS). The authors showed that the ignition delay behavior with the temperature fluctuations changes depending on the mean temperature value and the NTC regime of the fuel. Thus, if fluctuations are increased, the ignition delay increases for a mean temperature lower than the NTC zone, while it decreased for a mean temperature higher than the NTC zone. For a mean temperature value within the NTC zone the ignition delay increases for small fluctuations but it decreased for large fluctuations. Furthermore, Yoo et al. also studied the effects of the turbulence timescale on the ignition. Thus, fast turbulence timescale homogenizes the mixture leading to a faster ignition propagation, while longer turbulence timescales are not able to homogenize the temperature and the ignition propagation occurs mainly by deflagration. However, the effect of the turbulence timescales on the ignition delay is almost negligible compared to that of thermal stratification. Similar DNS studies have been performed by Bansal and Im [14]. However, analyses under engine-like conditions have to be carried out in order to understand the autoignition propagation phenomenon in a real engine.

Chemiluminescence is a non-intrusive optical technique widely used in combustion diagnosis [15], which has shown to be able to describe the different phases of the combustion process under HCCI conditions [16]. For instance, Dubreuil et al. [17] studied the global effect of the EGR on the HCCI combustion of n-heptane in a transparent single-cylinder diesel engine for two EGR rates for a certain equivalence ratio by means of OH^* chemilumines-

4

cence. By observing cool and main flame emissions, the authors found that EGR delays and degrades the combustion phenomenon. They also proved that the natural emissions of combustion are sufficiently sensitive to allow the analysis of the combustion process. Finally, the authors observed that the increase of the EGR rate decreases the OH^* radiation, which is linked to the reduction of the global combustion reactivity. This optical technique has been also widely used to study the heterogeneities that cause sequential autoignition. For example, Liu et al. [18] have used chemiluminescence to study the heterogeneities present in HCCI combustion under different injection strategies and cooling fluid temperatures, comparing their results to CFD calculations.

In this study, the autoignition propagation under HCCI conditions is described from a phenomenological point of view. To do so, chemiluminescence measurements have been performed in a Rapid Compression Expansion Machine (RCEM) using iso-octane and n-heptane, which are typical surrogate fuels for gasoline and diesel fuel, respectively. The velocity of propagation of the reaction front is experimentally obtained under different conditions of pressure, temperature, equivalence ratio and oxygen mass fraction. Finally, different Damköhler numbers have been evaluated in order to characterize the phenomenon, which are theoretically explained in this paper.

The structure of the paper is the following: first, the experimental facilities involved in this study are described, as well as the methodological approach, which includes the post-processing procedure and the parametric study performed. Then, the phenomenological analysis of the autoignition propagation phenomenon is explained. Afterwards, the phenomenological

5
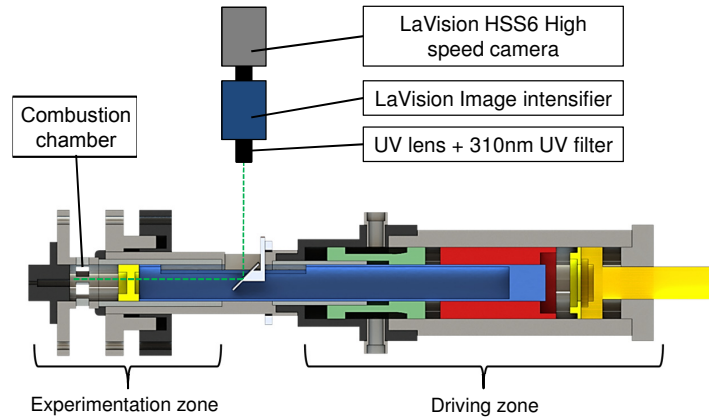
Figure 1: Schematic of the Rapid Compression Expansion Machine, including the optical setup.

description is evaluated by means of OH* chemiluminescence experimental results. Finally, the conclusions of this study are shown.

2. Materials and methods

2.1. RCEM

An RCEM is an experimental facility usually used in autoignition studies due to its capability to reproduce the engine compression and expansion strokes under fully controlled initial and boundary conditions [19]. The experimental results used in this investigation have been obtained by Desantes et al. [20] in a previous work, while the raw results have been re-processed in order to obtain data about the autoignition propagation. Therefore, a brief summary about the RCEM characteristics is presented in the following paragraphs, while a more detailed description about the experimental facility and the experimental methodology can be found in [20].

A schematic of the RCEM is shown in Fig. 1. The piston position and, thereby, the volume of the combustion chamber are measured by an AMO LMK102 incremental position sensor (0.01 mm of resolution). Besides, the in-cylinder pressure is measured by a Kistler 7061B cooled piezo-electric pressure sensor (-80 pC/bar of sensitivity), which is coupled to a Kistler 5011 charge amplifier. Different Wika piezo-resistive pressure sensors are available to control the filling of the combustion chamber (0.01 bar of resolution). The injection system is composed by a Siemens hollow cone piezo-injector with a cone angle of 90°, the fuel delivery rate of which has been previously characterized with an IAV injection rate analyzer. The instantaneous signals (including the control and synchronization signals, as for example the camera triggers) have been recorded at 100 kHz with a PC-based transient measurement recorder. The RCEM is filled from an external tank that can be heated up to 373 K. The synthetic EGR is produced in the tank by a filling based on partial pressures where N_2, CO_2 and O_2 can be used, while its exact composition is checked in a Horiba PG-250 portable gas analyzer. In this study, EGR was considered as the products of a complete combustion reaction between the fuel and dry air in which the amount of oxygen is the one desired by the user, as explained in [21]. The combustion chamber is scavenged several times before the filling to avoid the contamination of the mixture by residual gases, while the fuel is directly injected into the combustion chamber at the beginning of the intake process to avoid problems of stratification. Besides, it has been checked in previous unpublished CFD calculations that the duration of the filling procedure ($\approx$40 s) is enough to guarantee a homogeneous environment in the chamber when the compression

7

stroke starts.

The experimentation piston is composed by a steel-made piston with a 84 mm bore and a quartz-made bowl with cylindrical shape, 50 mm of bore and 2 mm in depth, which allows the axial optical access. The flat bowl ensures that the chamber is recorded without any image distortion, while a 45° tilted mirror allows a direct view of the combustion chamber through the transparent bowl. A schematic of the optical setup is shown in Fig. 1. A 12-bit LaVision HighSpeedStar 6 camera coupled to a LaVision HighSpeed IRO intensifier equipped with a 100 mm focal length $f = 2$ UV objective (by Bernhard Halle Nachfolger GmbH) were used for image acquisition. Additionally, a 310 nm interference filter (FWHM=10 nm) was used to eliminate any additional radiation outside the OH* radical wavelength. An acquisition frequency of 30 kHz has been chosen in order to capture the combustion evolution. An exposure time of 33 μs and a rectangular image of 384x448 pixels allow to see the whole window with a pixel/mm ratio of 6.89. The maximum exposure time has been selected in order to use lower gain values and, therefore, reducing the image noise.

Thanks to the good repeatability of the ignition event, only 5 repetitions had to be performed for each operating condition to ensure representative measurements of the ignition delay. In fact, the semi-amplitude of the confidence interval with a level of confidence of 95% is smaller than 1% of the mean ignition delay value by performing 5 experiments per point. Specifically, the ignition delay in the experimental facility is defined as the time between the start of the rapid compression process and the instant in which the maximum pressure rise is obtained.
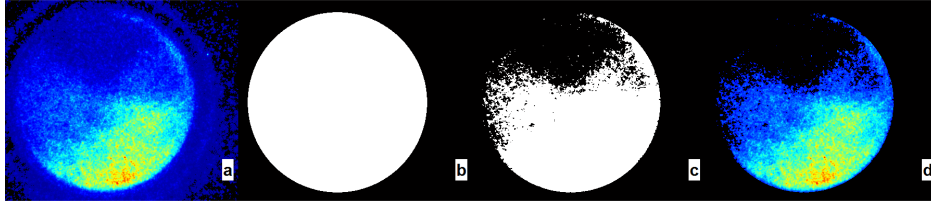
Figure 2: Processing sequence for raw image (a), geometrical mask (b), intensity mask (c) and final image (d).

Finally, the in-cylinder average temperature profile is calculated for each experiment by applying the equation of state, while the heat release is obtained by the energy equation. Heat losses are characterized by a model based on the Woschni correlation [22], and the calculations include two additional models for deformations and leaks, both of them explained in [23, 24].

2.2. OH* chemiluminescence imaging

The raw images obtained by Desantes et al. [20] have been processed in the present study by an in-house developed routine in MATLAB. The processing algorithm starts calculating the maximum pixel intensity of each frame in order to determine the useful dynamic range of the image sequence. Then, a background noise level, I_{back}, is obtained by averaging 100 images where there is no presence of OH* luminosity. The probable error of the noise is calculated assuming a normal distribution of the noise radiation as $\gamma = 0.6745\sigma$, where σ represents the standard deviation. If the maximum pixel intensity of a certain image is lower than four times the probable error of the noise, the radiation belongs to noise and the image is not processed.

The useful images are filtered by applying two masks, one based on the

9

window geometry and one based on the intensity of the radiation. Fig. 2-a shows a raw image in which reflections can be seen outside the window. A 50 mm of bore geometrical mask (Fig. 2-b) is applied in order to discard the light reflected by the piston and cylinder walls. A second mask (Fig. 2-c) is designed using the maximum pixel intensity of each image, I_{max}, and the averaged background intensity I_{back}, obtaining the threshold as $I_{back} + p(I_{max} - I_{back})$, where p is a percentage. Thus, all the pixels the intensity of which is lower than this threshold are considered as noise. Finally, the filtered image excludes all the background noise and reflected light, as shown in Fig. 2-d.

The velocity of propagation of the autoignition front is now calculated from the images. Desantes et al. [20] have shown that the OH* radiation can be outshined by the CO continuum radiation under HCCI conditions, so that the luminosity recorded in the experiments can belong to OH* or to CO depending on the combustion temperature. However, the position of the reaction front can be determined by both OH* or CO-to-CO_2 radiation, since both are good tracers of the high temperature combustion [25]. Furthermore, since 2-D imaging is applied on a 3-D phenomenon, the radiation recorded by the camera is an integrated value of the whole volume and not a single first plane acquisition. Thus, the intensity gradients in the axial direction could have some effect on the filtering of the images to obtain the velocity of propagation, since small isolated high-intensity volumes could be ignored. Nevertheless, the existence of high-intensity single points is very unlikely under HCCI conditions.

The velocity of propagation is obtained by averaging the perimeter incre-
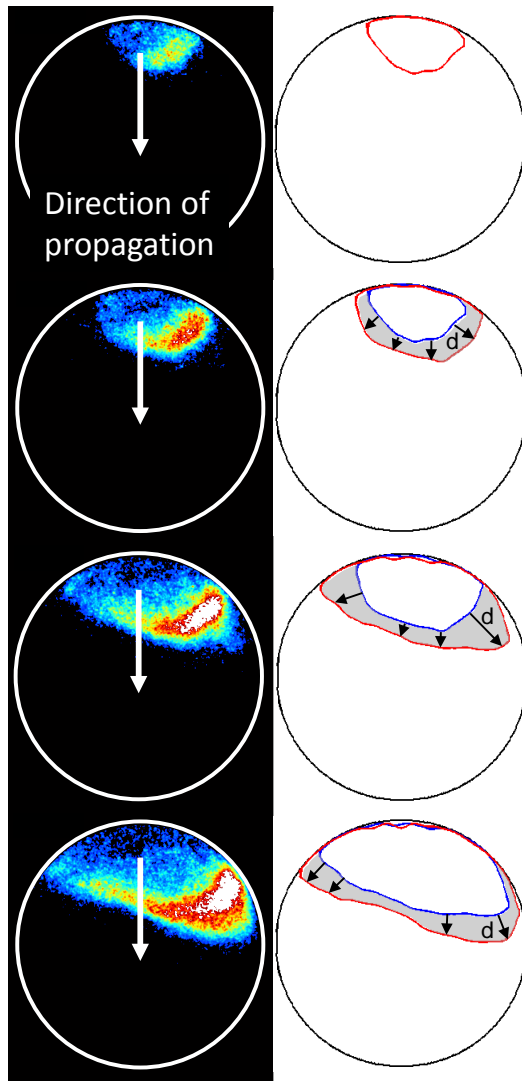
Figure 3: Sequential autoignition caused by the cooled piezo-electric pressure sensor located at the bottom of the cylinder head.

ment between two consecutive images. The sequential autoignition is promoted by the temperature distribution in the combustion chamber, since the cooled piezo-electric pressure sensor leads to a cold spot at the bottom of the cylinder head, resulting in a hot spot at the top, which originates the ignition. Thus, the autoignition propagation occurs always from the top to the bottom side of the combustion chamber, as shown in Fig. 3 to the left. For a certain image, the reaction front, which is obtained avoiding isolated pixels, is filtered in order to easily obtain the normal distance between fronts for two consecutive images, as shown in Fig. 3 to the right. Thus, the velocity of propagation is calculated as $u_{prop} = \bar{d}/\Delta t$, where $\bar{d}$ represents the averaged normal distance between two consecutive fronts.

Finally, sensitivity analyses, the result of which can be seen in Appendix A, have shown that the propagation velocity does not depend on the percentage, p, used for filtering the images for values of p between 8% and 18%, which lead to approximately the same values of u_{prop}. Specifically, $p = 10\%$ has been chosen in this study.

2.3. CFD calculations

A CFD dynamic simulation of the RCEM compression stroke under motoring conditions has been carried out in ANSYS Fluent in order to estimate the turbulent thermal diffusivity, the turbulent kinematic viscosity and the temperature gradients when the ignition occurs.

The combustion chamber has been modeled in SolidWorks and the CAD model has been exported to ANSYS Fluent for its discretization. A non-conforming mesh is used, in which, after a grid size sensitivity analysis, the maximum cell size is kept to 1 mm for the gas core, while it is reduced

12

up to 0.5 mm near to the walls (Δr=2 mm) and in the bowl. The turbulence model applied in the simulations is the k-ϵ standard, while a constant time step equal to $3.3 \cdot 10^{-5}$ s has been selected, which corresponds to a $\Delta\theta = 0.2$ CAD. Finally, the initial and boundary conditions have been imposed in order to replicate the RCEM behavior. The mesh is deformed in order to adapt the cells to the piston movement. The mesh deformation is obtained by means of the Dynamic Layering Method, in which both the split factor and the collapse factor are equal to 0.4.

A RANS model assumption mainly affects the estimation of the temperature gradient, which defines the ignition delay gradient and, therefore, the chemical velocity of the autoignition front. Despite the fact that a RANS approach artificially model the turbulent fluctuations, Sjöberg et al. [9] experimentally showed that the sequential autoignition under HCCI conditions is mainly controlled by the temperature gradients generated in the chamber by heat losses and wall effects. Therefore, the temperature fluctuations present in the turbulent micro-scale seem to have a minor role and their determination is not critical.

A detailed description about these CFD simulations can be found in [26].

2.4. Parametric study performed

The performed experimental study, which can be seen in Table 1, was as follows:

- Fuel: iso-octane and n-heptane.

- Initial temperature (T_0): 358K (only for n-heptane), 383K, 408K, 433K and 458K.

- Initial pressure (P_0): 1.4bar and 1.7bar.

- Compression stroke: 249mm.

- Compression ratio (CR): 15 and 17.

- Oxygen mass fraction (X_{O_2}): 0.21 (0% EGR), 0.147 (30% EGR), 0.126 (40% EGR) and 0.105 (50% EGR).

- Equivalence ratio (Fr): from 0.3 to 0.8 depending on the fuel and on the oxygen mass fraction.

The operating point $(X_{O_2}=0.126$, $Fr=0.4)$ has been chosen as base point in order to be able to try more and less reactive mixtures without damaging the facility. Besides, it should be noted that the initial temperature is always above the boiling point of the fuel, ensuring that the fuel is in vapor phase before the beginning of the cycle.

		X_{O_2} [-]			
		0.21	**0.147**	**0.126**	**0.105**
T_0 [K]	**358**	*0.4*	*0.4*	*0.3, 0.4, 0.5, 0.6*	*0.4*
	383			0.4, 0.5	0.4
	408	0.3, 0.4	0.3, 0.4	0.3, 0.4, 0.5, 0.6, **0.7**, **0.8**	0.3, 0.4, 0.5, 0.6, **0.7**, **0.8**
	433			0.4, 0.5	0.4
	458	**0.4**	**0.4**	**0.3**, 0.4, 0.5, **0.6**	0.4

Table 1: Parametric study performed for pure n-heptane and iso-octane. Equivalence ratio for different initial temperature values and oxygen molar fractions. *Italic.-* exclusively for n-heptane. **Bold.-** exclusively for iso-octane.

3. Theory and calculations

A phenomenological model to explain the autoignition propagation, so called sequential autoignition or propagation of the reaction front, under HCCI conditions is described in this section. To do so, the combustion chamber is assumed to be composed by two different fluids, burned gases (indicated by the subscript b) and unburned mixture (indicated by the subscript u). The burned fuel is calculated by means of the cumulated heat release and the reaction heat of the global combustion reaction. Thus, the amount of each compound can be obtained by solving a mass balance. First, the temperature of the unburned mixture is obtained assuming a polytropic evolution starting from the ignition point. Then, the temperature of the burned gases is obtained by solving an energy balance in the combustion chamber. Further details about this procedure can be found in [27].

Different characteristic physical and chemical velocities are evaluated, defining the following Damköhler numbers:

$$Da_1 = \frac{u_{prop} - u_b}{u_b} \tag{1}$$

$$Da_2 = \frac{u_{prop} - u_b}{a} \tag{2}$$

$$Da_3 = \frac{u_{prop} - u_b}{u_{TC}} \tag{3}$$

where u_{prop} is the velocity of propagation of the autoignition front, which is an apparent chemical velocity experimentally measured while u_b is the mean expansion speed of the burned gas. Thus, the combustion speed of the reaction front is equal to $u_{comb} = u_{prop} - u_b$. Besides, $a = \sqrt{\gamma_u R_g T_u}$ represents the speed of sound, where γ_u is the adiabatic coefficient of the unburned gas,

15

$R_g = R/MW_u$ is the gas constant of the unburned gas (universal gas constant divided by the molecular weight of the unburned gas) and T_u is the unburned gas temperature. Finally, u_{TC} represents the turbulent combustion velocity of a flame front dominated by diffusive effects.

The dimensionless number Da_1 relates the combustion velocity associated to the reaction front with the mean expansion speed of the burned gas. Thus, Da_1 quantifies the relevance of expansion effects on the propagation velocity. If $Da_1 >> 1$, the expansion of the burned gases caused by the pressure rise associated to the combustion process is negligible compared to the combustion velocity, which means that the propagation of the reaction front is controlled by the chemical kinetics of the mixture.

The dimensionless number Da_2 relates the combustion velocity associated to the reaction front with the speed of sound. Thus, Da_2 quantifies the relevance of pressure gradients in the chamber (pressure waves based phenomena). If $Da_2 << 1$, pressure waves propagate much faster than the reaction front and constant pressure can be assumed in the chamber (null pressure gradients), otherwise, the existence of pressure waves has to be taken into account.

The dimensionless number Da_3 relates the combustion velocity associated to the reaction front with the turbulent combustion velocity obtained of a flame front dominated by diffusive effects. Da_3 quantifies the relevance of diffusion on the autoignition propagation. If $Da_3 >> 1$, the reaction front propagates much faster than a typical flame front, meaning that mass and thermal diffusion have no influence on the autoignition (diffusion phenomena are too slow), otherwise, the diffusion from the reaction front to the unburned

16

mixture has to be taken into account.

The mean expansion speed of the burned gas, u_b, is calculated from the variation of unburned mixture mass as follows [28]:

$$u_b = \frac{V_u}{\gamma_u P A_f} \frac{dP}{dt} \tag{4}$$

where V_u is the unburned mixture volume and A_f is the area of the reaction front. Since the ignition is promoted by a hot spot located at the top of the combustion chamber that acts as a spark, a spherical shape reaction front can be assumed, the volume of which is the volume of the burned gases (obtained from their mass and thermodynamic conditions, derived as explained above). Thus, the radius of the equivalent sphere is obtained from the burned volume, V_b, and the area of the reaction front is calculated from such equivalent radius:

$$A_f = 4\pi \left(\frac{3V_b}{4\pi}\right)^{2/3} \tag{5}$$

The turbulent combustion velocity, u_{TC}, is calculated from the laminar burning velocity of a flame, u_{LC}, using the Schelkin's scaling law: $u_{TC}/u_{LC} \propto \sqrt{1 + \nu_T/\nu} \approx 32$, where ν_T/ν is the turbulent-to-molecular kinematic viscosity ratio, which is estimated at 10^3 at TDC by CFD calculations. Besides, the laminar burning velocity is calculated by means of the Metghalachi-Keck correlation for iso-octane [29]:

$$u_{LC} = \left(0.2632 - 0.8472 \left(Fr - 1.13\right)^2\right) \left(\frac{T_u}{298}\right)^{2.18 - 0.8(Fr-1)} \cdot$$
$$\cdot \left(\frac{P}{1.01325}\right)^{-0.16 + 0.22(Fr-1)} (1 - 2.1 Y_{EGR}) \tag{6}$$

where Fr is the working equivalence ratio, T_u is the temperature of the unburned mixture in K, P is the pressure in bar and Y_{EGR} is the mass fraction of the inert diluent (in case of working with synthetic EGR). Despite the fact that Eq. 6 has been experimentally validated only up to 50.7 bar and 700 K, extrapolations can be performed to obtain estimators of the turbulent combustion velocity, since orders of magnitude of Da_3 want to be obtained.

Finally, the autoignition propagation velocity is assumed to be a chemical velocity controlled by the chemical kinetics of the mixture, i.e., by the ignition delay distribution in the combustion chamber. Thus, the velocity of propagation of the reaction front can be estimated as [30]:

$$u_{chem} = \left(\frac{d\tau}{dx}\right)^{-1} \tag{7}$$

where τ represents the ignition delay under certain thermodynamic conditions and x represents the direction of propagation of the front (in this study, from the top to the bottom of the combustion chamber).

The ignition delay is obtained for each ignition condition by means of chemical simulations in CHEMKIN. The Curran's detailed chemical kinetic mechanism for iso-octane and n-heptane [31, 32], which consists of 1034 species and 4238 reactions, has been solved in a homogeneous closed reactor (perfectly stirred reactor, PSR), which works with constant pressure and

18

uses the energy equation to solve the temperature temporal evolution. This mechanism has been widely validated versus experimental measurements in previous works [33, 34]. Ignition is defined as the instant at which the maximum temperature rise rate occurs and the resulting ignition delays have been parameterized using the Levenberg-Marquardt algorithm for minimizing the sum of the squares of the deviations. The least-squares curve fitting results in the following expressions for iso-octane (Eq. 8) and n-heptane (Eq. 9), respectively:

$$\tau_{iso-oct} = 6.2697 \cdot 10^{-11} P^{-0.504} X_{O_2}^{-1.946} Fr^{-0.836} exp\left(\frac{14940}{T}\right) \tag{8}$$

$$\tau_{n-hep} = 1.5931 \cdot 10^{-6} P^{-1.316} X_{O_2}^{-1.637} Fr^{-0.548} exp\left(\frac{8756}{T}\right) \tag{9}$$

where the ignition delay, τ, is in seconds. P is the pressure in bar, Fr is the working equivalence ratio, X_{O_2} is the oxygen molar fraction and T is the temperature in K. The fitting accuracy is shown in Appendix B.

Assuming that the sequential autoignition is caused by the temperature gradient under HCCI conditions [9], the chemical velocity can be finally obtained as:

$$u_{chem} = \left(\frac{d\tau}{dT}\frac{dT}{dx}\right)^{-1} = \left(-\tau\frac{T_a}{T^2}\frac{dT}{dx}\right)^{-1} \tag{10}$$

where T_a represents the activation temperature, which is equal to 14940 K for iso-octane and to 8756 K for n-heptane. Furthermore, the temperature gradient, dT/dx, has been estimated in -160 K/m by means of CFD calculations.

19

Finally, the velocity ratio u_{chem}/u_{comb}, where $u_{comb} = u_{prop}-u_b$ is obtained from experimental measurements, as a way to evaluate the phenomenological description shown in this section and that will be discussed below.

4. Results and discussion

The results derived from this investigation are presented in this section. First, the experimental measurements are shown and analyzed, including trends and variability. Secondly, the phenomenological model described in Section 3 is applied and the relevance of the different phenomena involved in the autoignition propagation is discussed.

4.1. Experimental measurements

Fig. 4 shows the maximum combustion velocity of the autoignition front versus the maximum in-cylinder average temperature (Fig. 4 to the left) and versus the ignition time referred to TDC, $t_i - t_{TDC}$, (Fig. 4 to the right) for iso-octane (top) and n-heptane (bottom). Despite the fact that the reaction front propagation is controlled by the thermodynamic conditions reached at the instant of ignition, the ignition time is controlled by the successive thermodynamic conditions reached during the ignition delay. Thus, for a certain engine configuration, the propagation velocity is mainly controlled by the ignition delay under constant conditions, τ, evaluated at the thermodynamic conditions of the ignition point. It can be seen that the higher the maximum temperature reached the faster the combustion velocity. However, earlier ignitions are not necessarily related to a faster propagation. The propagation velocity increases if the ignition is advanced for iso-octane, since the smooth NTC behavior of this fuel causes that the higher the reactivity (the earlier

20

the ignition), the shorter the ignition delay at the ignition conditions and the faster the autoignition propagation. Nevertheless, the strong NTC behavior of n-heptane (which is described in [21]) can lead to longer ignition delays at ignition conditions even if the global reactivity is increased (earlier ignitions). Finally, Fig. 4 shows, in red, the effect of the equivalence ratio on the combustion velocity, while it shows the effect of the oxygen concentration in blue. It can be seen that the higher the equivalence ratio or the higher the oxygen content (the higher the reactivity under LTC conditions), the faster the propagation.

The repeatability of the phenomenon has been studied in order to identify if the variability of the results is caused by physical aspects or if it is promoted by the measurement methods. Thus, the semi-amplitude of the confidence interval with a 95% of level of confidence, μ, has been calculated for the maximum propagation velocity, u_{prop}, for the corresponding pressure rise rate, dP/dt, and for the ignition delay, t_i, as a way to evaluate the cycle-to-cycle variation. Fig. 5 shows the values of μ normalized by the averaged maximum propagation velocity, the averaged pressure rise rate, and the averaged ignition delay respectively, versus the ignition time referred to TDC, $t_i - t_{TDC}$, for both fuels. It can be seen that, while the ignition delay has a very good repeatability, the sequential autoignition shows very high variability. In fact, the mean value of $\mu/\bar{x}$ has been calculated for the propagation velocity, the pressure rise rate and the ignition delay, for iso-octane and n-heptane, the results of which are summarized in Table 2. This is an expected result, since the autoignition propagation is controlled by combustion, which is a source of turbulence and, therefore, which has a random
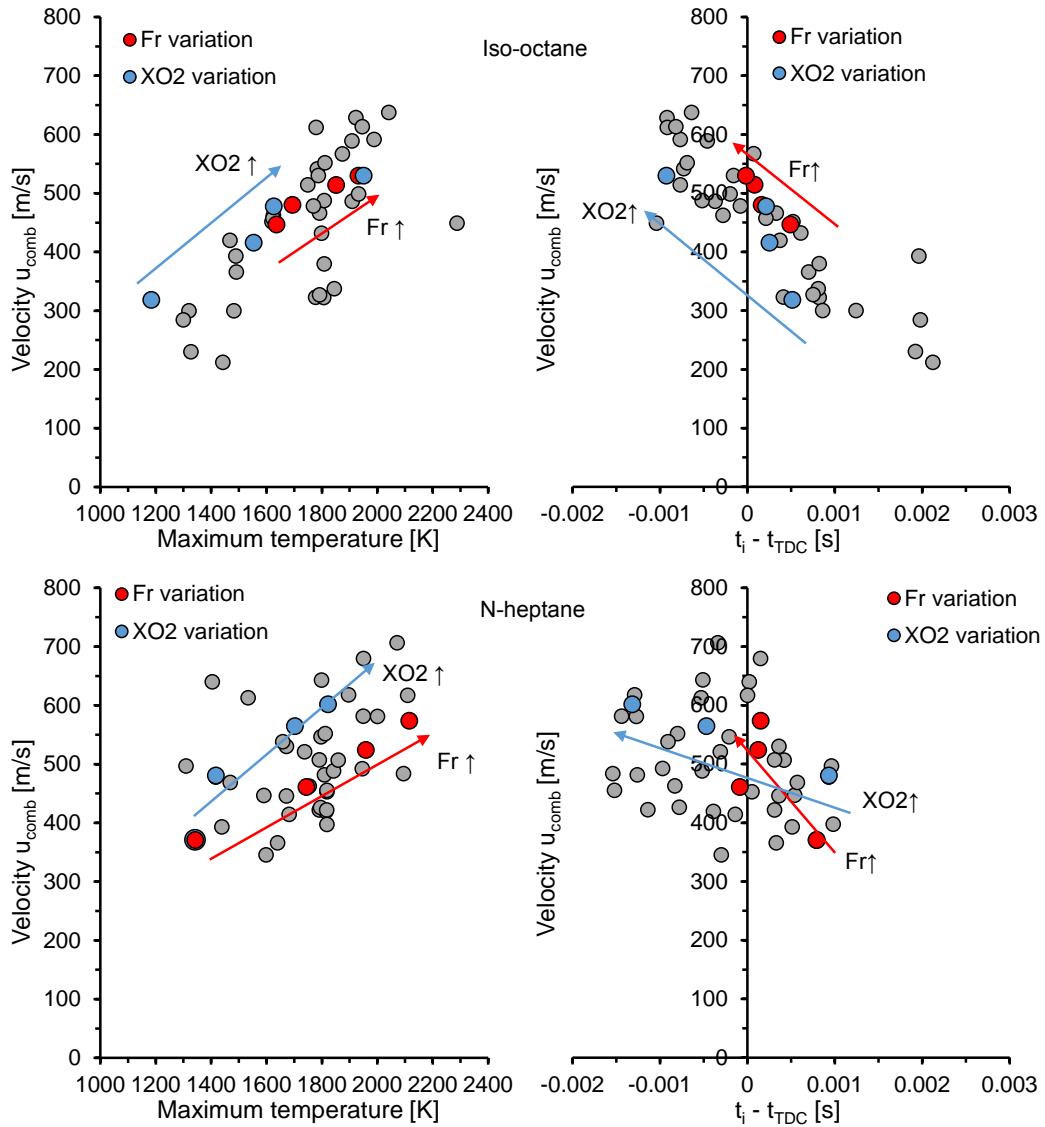
21

Figure 4: Maximum combustion velocity of the autoignition front. Left.- versus the maximum in-cylinder average temperature. Right.- versus the ignition time referred to TDC, $t_i - t_{TDC}$. Top.- iso-octane, Fr$\epsilon\{0.5, 0.6, 0.7, 0.8\}$ in red and $X_{O_2}\epsilon\{0.21, 0.147, 0.126, 0.105\}$ in blue. Bottom.- n-heptane, Fr$\epsilon\{0.3, 0.4, 0.5, 0.6\}$ in red and $X_{O_2}\epsilon\{0.21, 0.147, 0.126, 0.105\}$ in blue.
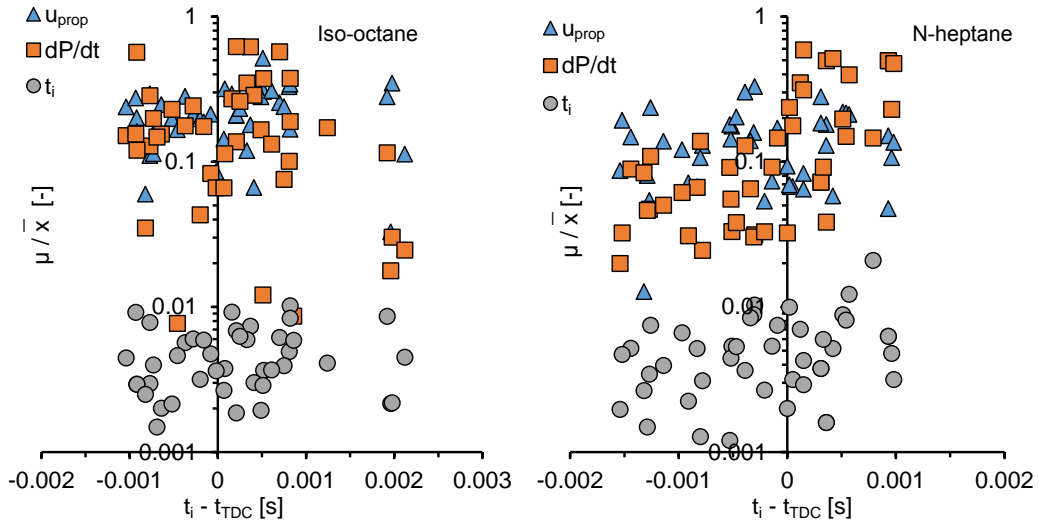
22

Figure 5: Semi-amplitude of the confidence interval with a 95% of level of confidence, μ, for the maximum propagation velocity, u_{prop}, the corresponding pressure rise rate, dP/dt, and for the ignition delay, t_i, normalized by the averaged values, $\bar{x}$, versus the ignition time referred to TDC, $t_i - t_{TDC}$. Left.- iso-octane. Right.- n-heptane.

behavior by definition. Moreover, the corresponding pressure rise rate shows the same repeatability than the combustion velocity, which means that such dispersion is intrinsic to the physical phenomenon and it is not caused by the post-processing. Moreover, Table 2 shows that the sequential autoignition of iso-octane has higher cycle-to-cycle deviation. As it has been explained above, iso-octane leads to more intense combustion events. Therefore, turbulence and the subsequent fluctuations of the local thermodynamic conditions are higher for this fuel, leading to poorer repeatability.

23

	Iso-octane	N-heptane
	Averaged $\mu/\bar{x}$	Averaged $\mu/\bar{x}$
Propagation velocity, u_{prop}	21.7%	13.7%
Pressure rise rate, dP/dt	19.2%	16.2%
Ignition delay, t_i	0.468%	0.539%

Table 2: Repeatability analysis of propagation velocity, pressure rise rate and ignition delay by means of the averaged value of $\mu/\bar{x}$ for iso-octane and n-heptane.

4.2. Application of the phenomenological model

In order to describe the sequential autoignition by a chemical propagation velocity, the question is what are the thermodynamic conditions in front of the reaction front, i.e., what thermodynamic conditions should be used to evaluate Eq. 10. To do so, diffusive and pressure-based effects are quantified by means of different Damköhler numbers. Fig. 6, 7 and 8 show the three aforementioned dimensionless Damköhler numbers defined in Section 3. It can be seen that $Da_1 >> 1$ for all cases, which means that, contrary to what occurs in spark-ignition engines, the propagation velocity of the reaction front is dominated and controlled by the chemical kinetics of the mixture. This is an expected result, since autoignition is characterized to be a chemically-controlled phenomenon.

It can be seen in Fig. 7 to the left that $Da_2 = u_{comb}/a$ increases if the maximum in-cylinder average temperature is increased, specially for iso-octane. Furthermore, Fig. 7 to the right shows that Da_2 follows similar trends than the combustion velocity and the luminous area. $Da_2 > 0.75$ is reached in most cases, meaning that pressure gradients in the combustion chamber have
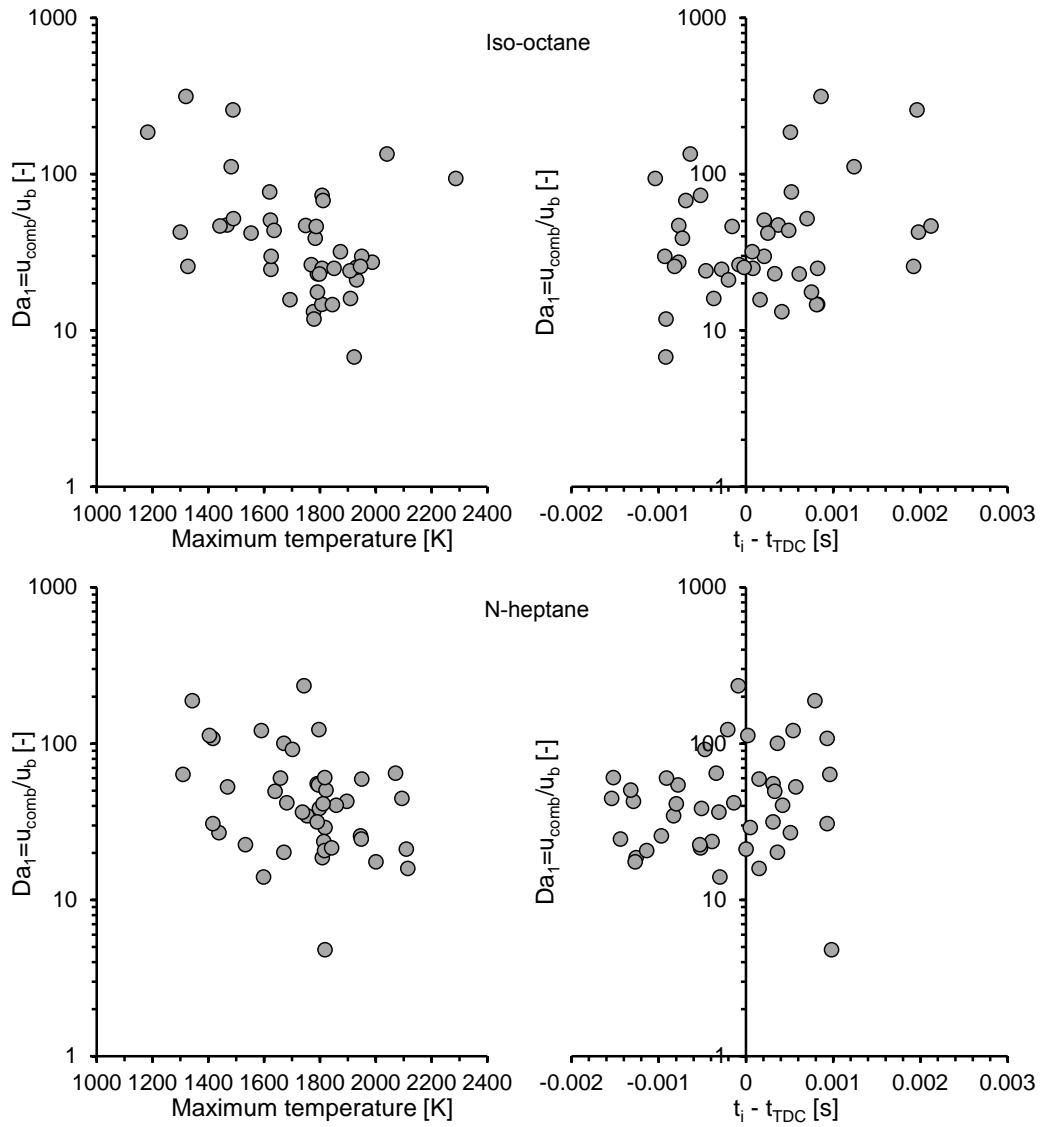
24

Figure 6: $Da_1 = u_{comb}/u_b$. Left.- versus the maximum in-cylinder average temperature. Right.- versus the ignition time referred to TDC, $t_i - t_{TDC}$. Top.- iso-octane. Bottom.- n-heptane.

to be taken into account.

Fig. 8 shows the same behavior for $Da_3 = u_{comb}/u_{TC}$ than for Da_2. However, $Da_3 > 4$ for all cases, meaning that diffusive effects are too slow compared to the propagation of the reaction front. Thus, the influence of mass and thermal diffusion on the autoignition propagation can be neglected under the conditions tested in this investigation. In fact, a critical propagation velocity of a flame front controlled by diffusive effects can be estimated, so that propagation velocities higher than the critical one imply that diffusive effects can be neglected. To do so, the temperature distribution from the burned gas to the unburned mixture is estimated by means of the hybrid theory of laminar flame propagation developed by Zeldovich and Frank-Kamanetsky and published by Semenov [35]. From this expression, the critical propagation velocity is estimated for the instant j taking into account the position of the reaction front at the instant $j + 1$ (from the propagation velocity experimentally measured) and assuming a difference between the temperature reached at this position and the temperature far away from the front of 1% ($\Delta T = 0.01 T_\infty$) as follows:

$$u_{crit} = \sqrt{-\frac{\alpha_T}{\Delta t} ln \left(\frac{0.01 T_\infty}{T_b - T_\infty} \right)} \in (43 - 55) \, [m/s] \tag{11}$$

where α_T represents the turbulent thermal diffusivity (estimated in 0.01 m^2/s at TDC from CFD calculations) and Δt is the experimental time step. Besides, T_b and T_∞ represent the temperature of the burning gas and the temperature far away from the reaction front, respectively. u_{crit} belongs to the range from 43 to 55 m/s in the present study, which means that, regarding
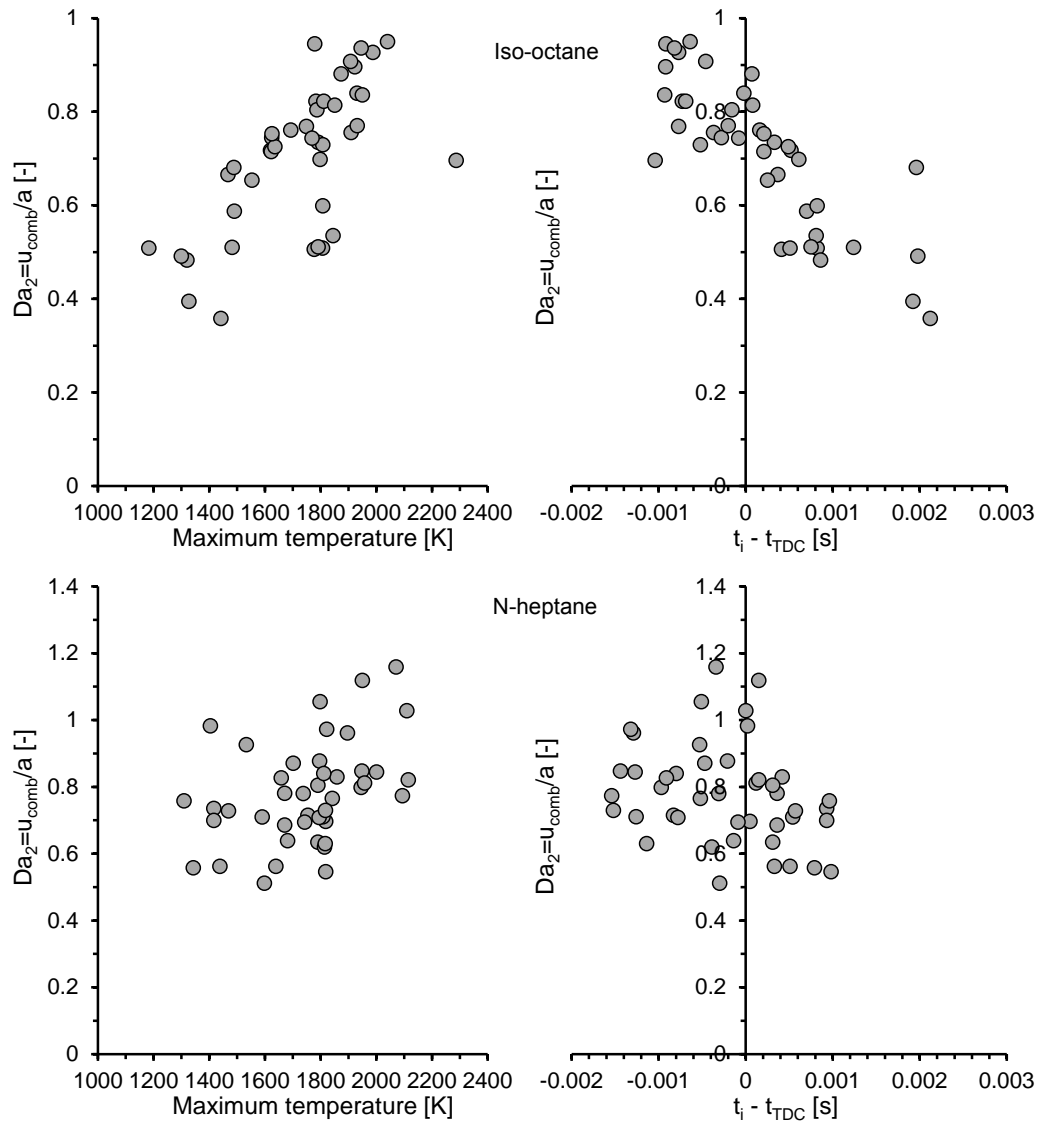
26

Figure 7: $Da_2 = u_{comb}/a$. Left.- versus the maximum in-cylinder average temperature. Right.- versus the ignition time referred to TDC, $t_i - t_{TDC}$. Top.- iso-octane. Bottom.- n-heptane.

Fig. 4, the reaction front propagates at T_∞ and diffusive effects are negligible. Finally, it should be noted that T_∞ has to be calculated from the temperature of the unburned mixture, T_u, taking into account the effect of the pressure waves generated in the chamber, as demonstrated by Da_2.

The chemical velocity that describes the autoignition propagation, u_{chem} (Eq. 10), has to be evaluated taking into account the thermodynamic conditions reached in front of the reaction front, which are affected by the pressure waves generated by the sequential ignition. Thus, three different scenarios have to be considered, all of them described in Fig. 9:

1. The incident pressure wave generated by the sequential ignition and the reaction front have the same propagation velocity. Therefore, the thermodynamic conditions used in Eq. 10 are the ones referred to the unburned mixture, as it is shown in Fig. 9 1.

2. The incident pressure wave generated by the sequential ignition is faster than the reaction front, but the reflected wave is not fast enough to interact with the reaction front. Therefore, the thermodynamic conditions used in Eq. 10 are the ones behind the incident pressure wave as it is shown in Fig. 9 2.

3. The incident pressure wave generated by the sequential ignition is faster than the reaction front and the reflected wave is also fast enough to interact with the reaction front. Therefore, the thermodynamic conditions used in Eq. 10 are the ones behind the reflected pressure wave as it is shown in Fig. 9 3.

The intensity of the incident pressure wave has to be estimated in order to evaluate the three different scenarios described above. Fig. 10 shows the raw
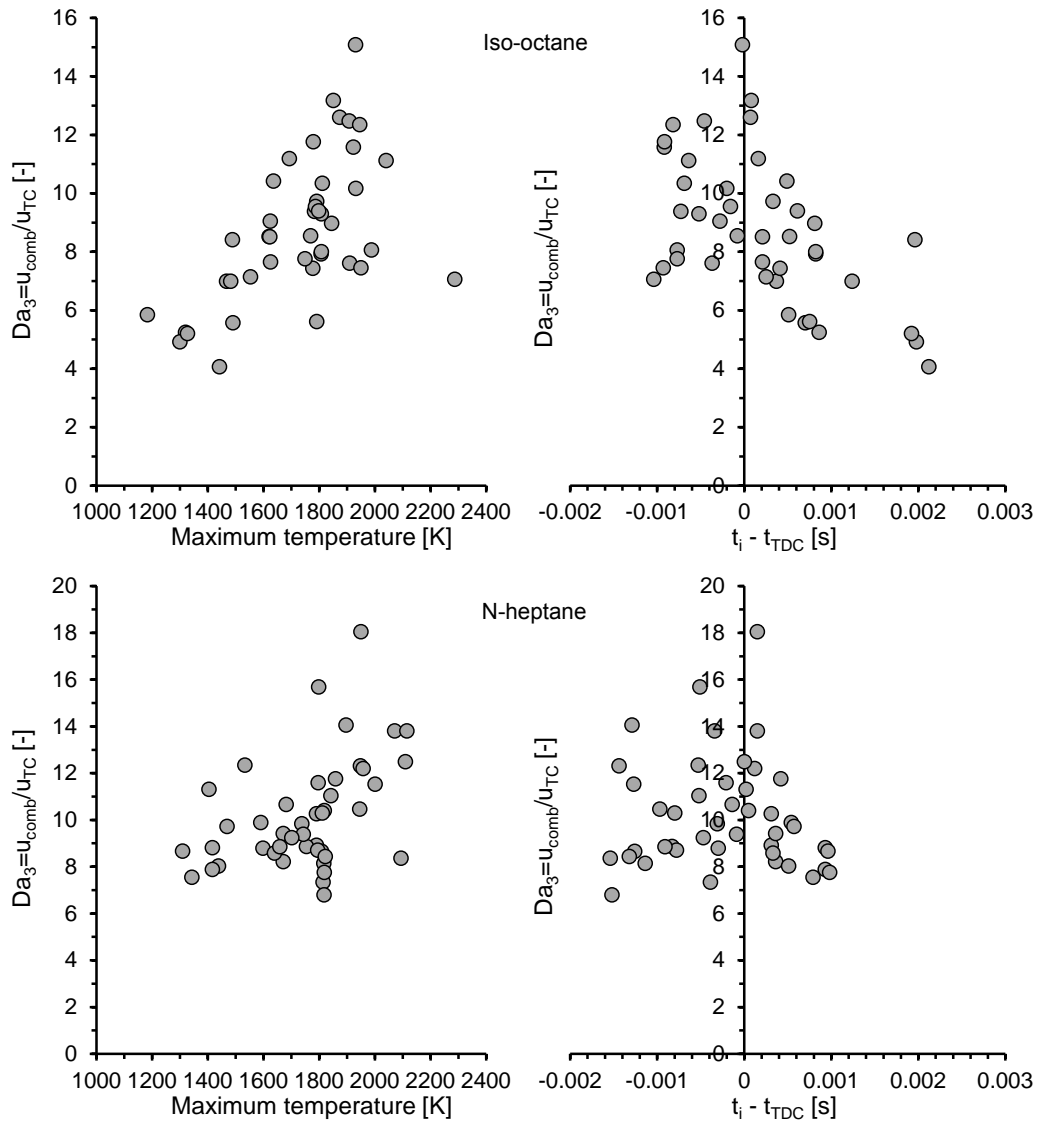
28

Figure 8: $Da_3 = u_{comb}/u_{TC}$. Left.- versus the maximum in-cylinder average temperature. Right.- versus the ignition time referred to TDC, $t_i - t_{TDC}$. Top.- iso-octane. Bottom.- n-heptane.
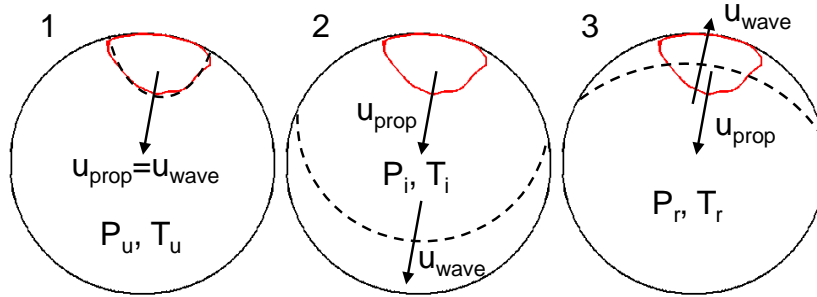
Figure 9: The three different scenarios that can be present in the combustion chamber. 1.-Reaction front and pressure front propagate together. 2.- The thermodynamic conditions established in front of the reaction front are controlled by the incident pressure front. 3.-The thermodynamic conditions established in front of the reaction front are controlled by the reflected pressure front.

in-cylinder pressure, its spectrum, and the filtered pressure waves for a certain case. It can be seen that 2000 Hz seems to be a proper value to decouple the pressure waves from the averaged in-cylinder pressure measured by the piezo-electric sensor. Since the sensor is located near the liner, the maximum measured pressure wave will be assumed to be an estimator of the pressure behind the reflected wave. Thus, the incident wave is indistinguishable, since the reflected wave is generated just on the sensor. However, the propagation velocity of the incident wave, the propagation velocity of the reflected wave and the intensity of the incident wave can be obtained by means of the Rankine-Hugoniot equations, since the pressure behind the reflected wave and the pressure in front of the incident wave are measured, as explained in Appendix C.

Fig. 11 shows the velocity ratio between the propagation velocities of the reaction front and of the incident pressure front. Points where $u_{prop}/u_{wave} =$
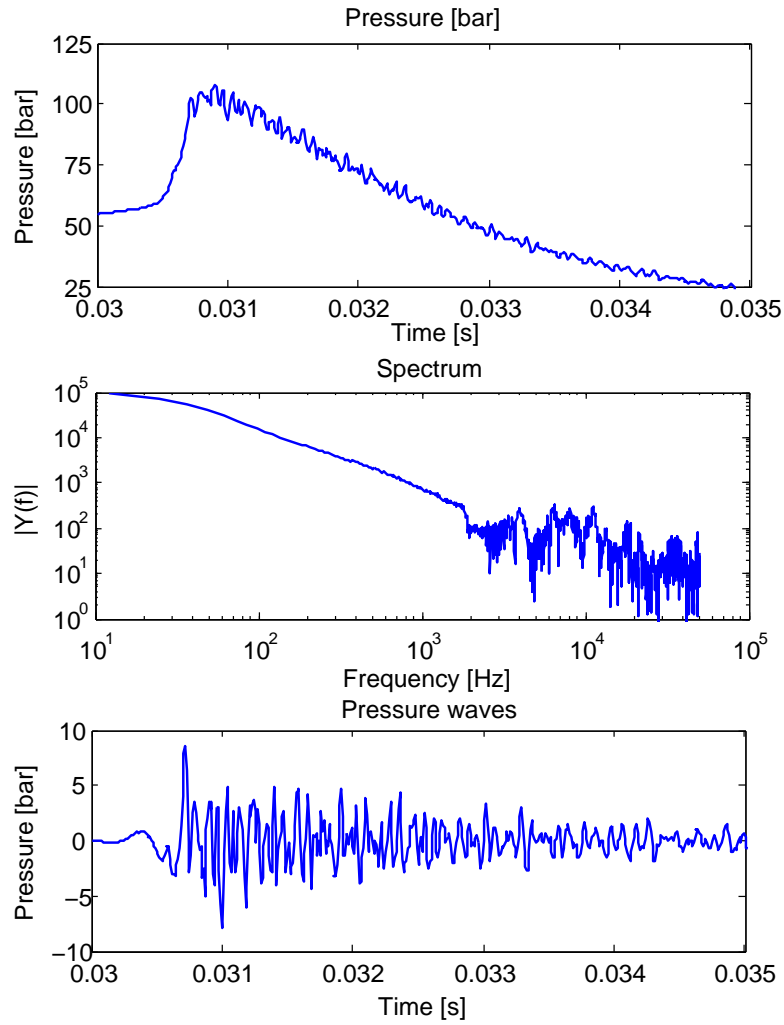
30

Figure 10: Raw in-cylinder pressure, its spectrum, and the filtered pressure waves for T_0=408K, P_0=1.4bar, CR=15, X_{O_2}=0.126 and Fr=0.5.
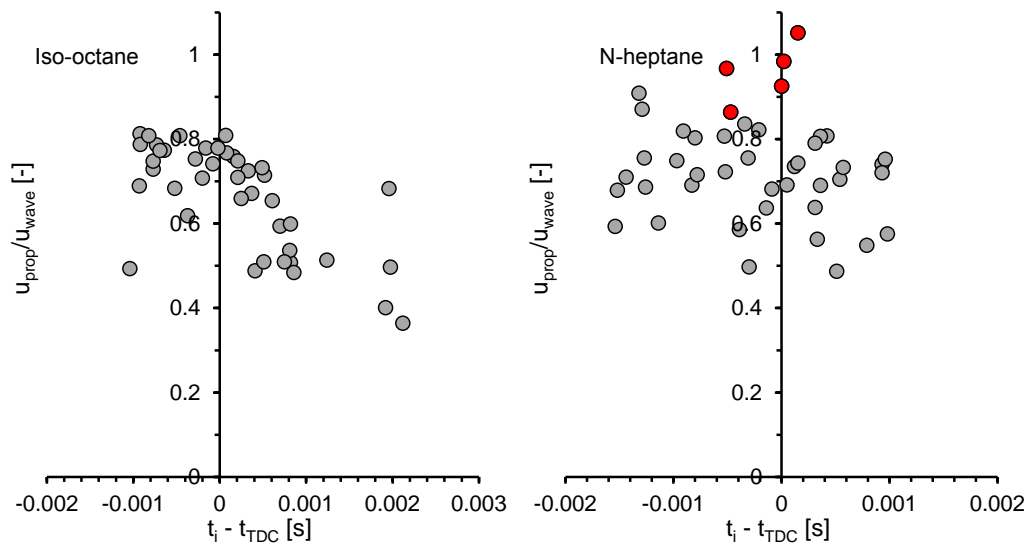
Figure 11: Velocity ratio, u_{prop}/u_{wave}, between the propagation velocities of the reaction front and of the incident pressure front versus the ignition time referred to TDC, $t_i - t_{TDC}$. Left.- iso-octane. Right.- n-heptane.

1, with a confidence interval with a level of confidence of 95%, are plotted in red, and the reaction front is assumed to propagate at the same velocity than the pressure front under these conditions. Thus, red dots in Fig. 11 represent detonations while grey dots represent deflagrations. Furthermore, it should be noted that the propagation velocity of the reaction front cannot be higher than the propagation velocity of the pressure waves generated by the combustion event, since the reaction front itself promotes new pressure fronts. It can be seen that detonations are only present for n-heptane, which shows higher propagation velocities. Furthermore, calculations show that in this study all deflagrations are affected by the incident pressure wave generated by the ignition but not by the reflected wave. Thus, the thermodynamic conditions (P_i, T_i) are the ones established in front of the reaction front for deflagrations and, therefore, the chemical velocity (Eq. 10) has to be evaluated using (P_i, T_i). In fact, the chemical velocity reaches values far away of the measurements if the pressure effects are not taken into account.

Fig. 12 shows the u_{chem}/u_{comb} ratio, where u_{comb} is obtained from the experimental results. It can be seen that most of the data are located in the interval [0.75, 1.25], which means that the autoignition propagation can be described by the chemical velocity affected by the incident pressure wave promoted by the sequential autoignition. It should be noted that incomplete combustion events as the ones that occurs during the expansion stroke lead to u_{chem}/u_{comb} ratio near to zero. This can be caused by the complexity in measuring the velocity of propagation, since very low radiation is recorded for these experiments. Furthermore, the ignition delay, τ, is more difficult to be predicted under these low-reactive conditions, leading to unrealistic u_{chem}
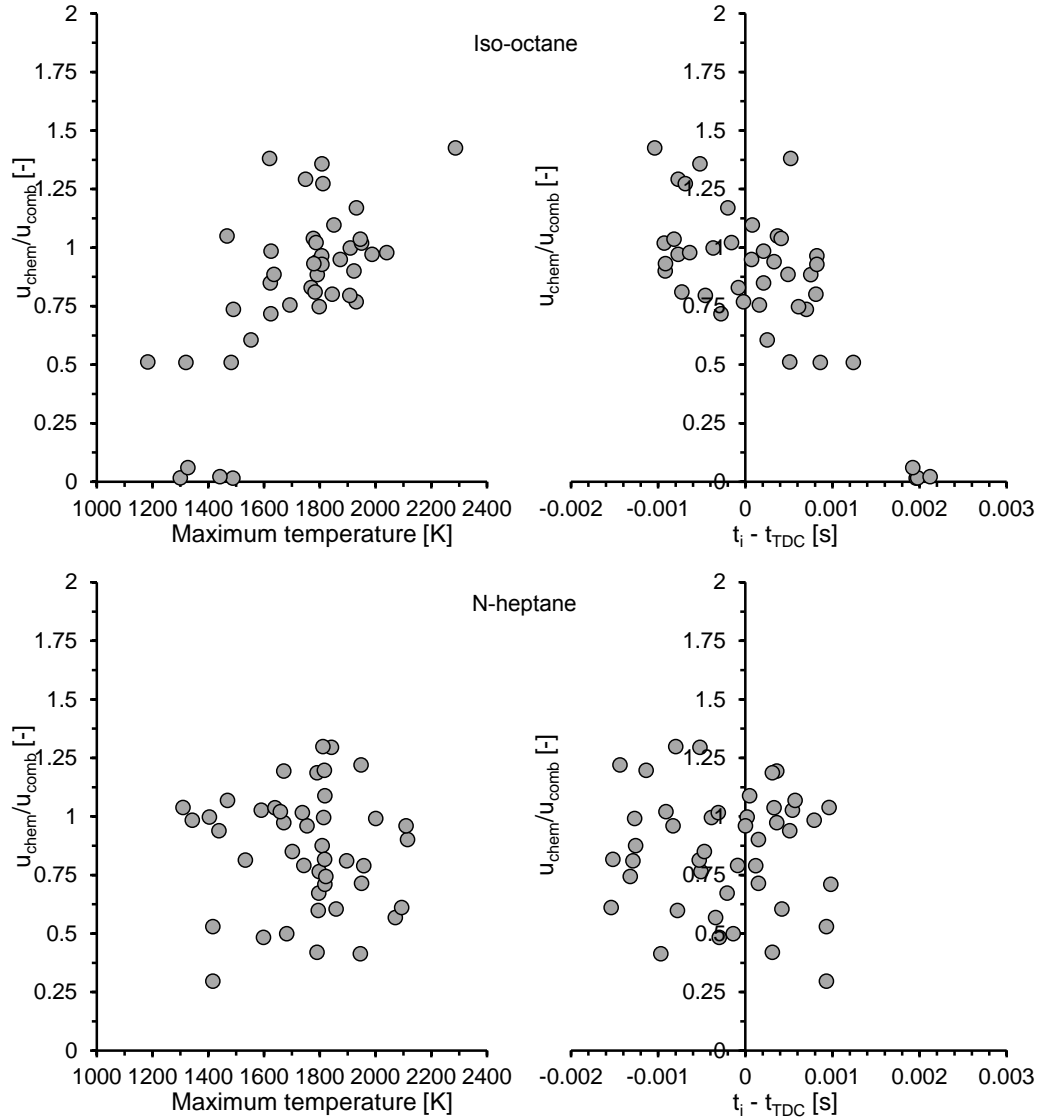
33

Figure 12: Velocity ratio, u_{chem}/u_{comb}, between the estimated and the measured combustion velocities of the reaction front. Left.- versus the maximum in-cylinder average temperature. Right.- versus the ignition time referred to TDC, $t_i - t_{TDC}$. Top.- iso-octane. Bottom.- n-heptane.

values. Finally, the high variability of the autoignition propagation phenomenon (Fig. 5) contributes also to obtain values for u_{chem}/u_{comb} different from 1.

5. Conclusions

In this work a phenomenological explanation about the autoignition propagation under HCCI conditions is developed. Diffusive effects from the burned zones to the fresh mixture, pressure waves based effects and expansion effects caused by combustion have been taken into account for the determination of the chemical velocity that describes the sequential autoignition. Besides, the relevance of each effect has been quantified by means of three different Damköhler numbers. Finally, the theoretical description has been compared to experimental propagation velocities obtained from chemiluminescence measurements in an RCEM.

The following conclusions can be deduced from this study:

- The maximum combustion velocity of the reaction front is controlled by the ignition delay, τ, evaluated at the ignition conditions, which is highly affected by the NTC behavior of the fuel. Thus, the earlier the ignition the faster the propagation of the reaction front for iso-octane, while a maximum of propagation velocity seems to occur near TDC for n-heptane.

- The sequential autoignition is characterized by very high variability, since it depends on the local conditions established by the combustion process. This leads to low repeatability, since combustion is a turbulent phenomenon and, therefore, it has a local random behavior.

35

- The sequential autoignition under HCCI conditions can be described by a chemical velocity, which is controlled by the thermodynamic conditions established in front of the reaction front by the pressure waves generated by the combustion phenomenon. In fact, the characteristic time of the autoignition propagation is too short to assume the absence of pressure gradients in the combustion chamber.

- On the one hand, expansion effects are negligible and, therefore, the measured propagation velocity and the combustion velocity of the reaction front are almost the same. On the other hand, the contribution of diffusive phenomena on the propagation is negligible, since the characteristic time of diffusion is too long compared to the characteristic time of the autoignition propagation.

Acknowledgements

Notation

a	Speed of sound
A_f	Area of the reaction front
b	Referred to the burned gases
CAD	Computer Aided Design
	Crank Angle Degree
CFD	Computational Fluid Dynamics
CI	Compression Ignition
CR	Compression Ratio
Da_1	Damköhler number referred to the expansion velocity
Da_2	Damköhler number referred to the speed of sound
Da_3	Damköhler number referred to the turbulent combustion velocity
DNS	Direct Numerical Simulation
EGR	Exhaust Gas Recirculation

37

Fr	Working equivalence ratio
$FWHM$	Full Width at Half Maximum
$HCCI$	Homogeneous Charge Compression Ignition
i	Referred to conditions behind the incident pressure wave
I_{back}	Luminous intensity of the background noise
I_{max}	Maximum pixel intensity of a certain image
LTC	Low Temperature Combustion
M	Mach number
MW	Molecular weight
NTC	Negative Temperature Coefficient
p	Percentage of luminous intensity to design the threshold that filters the images
P	Pressure
P_0	Initial pressure
$PPCI$	Partially Premixed Compression Ignition
PRF	Primary Reference Fuels
PSR	Perfectly Stirred Reactor
r	Referred to conditions behind the reflected pressure wave
R^2	Pearson's coefficient of determination
$RCEM$	Rapid Compression-Expansion Machine
SI	Spark Ignition
T	Temperature
T_0	Initial temperature

557

TDC	Top Dead Center	
t_i	Ignition delay under transient conditions	
u	Referred to the unburned mixture	
u_b	Expansion velocity of the burned gases	
u_{chem}	Chemical velocity	
u_{comb}	Combustion velocity of the autoignition front	
u_{LC}	Laminar combustion velocity	
u_{prop}	Propagation velocity of the autoignition front	
u_{TC}	Turbulent combustion velocity	
u_{wave}	Propagation velocity of the pressure front	
X_j	Molar fraction of the species j	
Y_j	Mass fraction of the species j	
α_T	Turbulent thermal diffusivity	
γ	Adiabatic coefficient	
μ	Semi-amplitude of the confidence interval with a 95% of level of confidence	
ν	Laminar kinematic viscosity	
ν_T	Turbulent kinematic viscosity	
τ	Ignition delay under constant conditions of pressure and temperature	

558

Appendix A. Sensitivity analysis of the effects of filtering on the computed propagation velocity

A sensitivity analysis about how the propagation velocity is affected by the filtering of the images has been performed. Each raw image is filtered by applying a filter that is designed using the maximum pixel intensity of the image, I_{max}, and the averaged background intensity I_{back}, obtaining the threshold as $I_{back} + p(I_{max} - I_{back})$, where p is a percentage. Thus, if the intensity of a certain pixel is lower than the threshold, this radiation is assumed to belong to the background noise and the intensity of the pixel is moved to zero.

The reaction front obtained from the images can be modified by changing the percentage, p, used in their filtering. Therefore, different thresholds will lead to different propagation velocities, which are obtained by means of the normal distance between reaction fronts of two consecutive images. Fig. A.13 to the left shows the propagation velocity evolution during the sequential autoignition process for T_0=408K, P_0=1.4bar, CR=15, X_{O_2}=0.126 and Fr=0.5, for six different values of p. It can be seen that the maximum propagation velocity can significantly change depending on the selected value of p. In fact, Fig. A.13 to the right shows the maximum propagation velocity for the six p values. It can be deducted from the figure that p should be properly selected to avoid unsuccessful results.

On the one hand, too high p values lead to a very severe filtering, which affects the low intensity images in a greater extent. Thus, if two consecutive
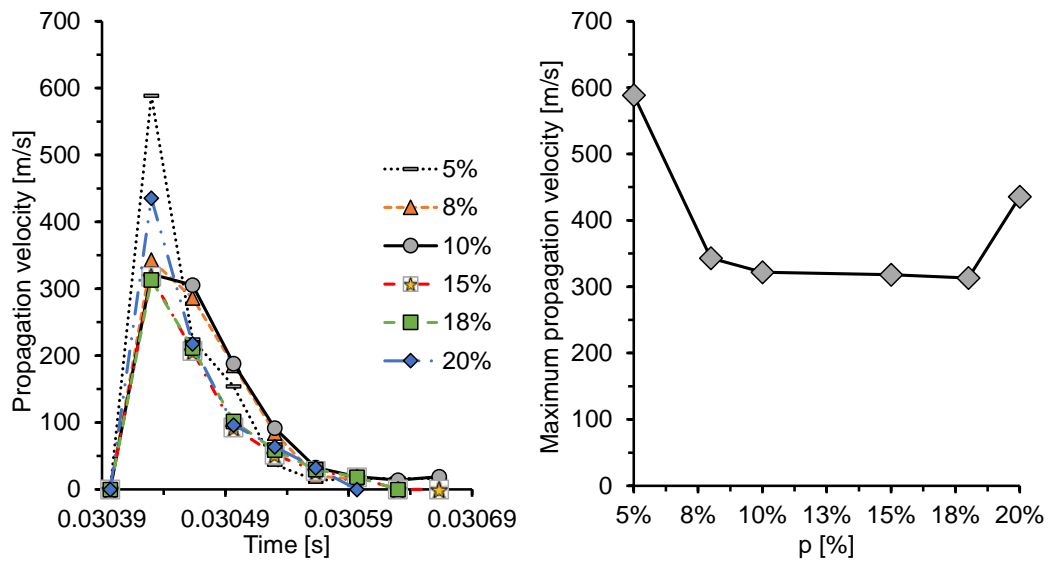
Figure A.13: Propagation velocity for T_0=408K, P_0=1.4bar, CR=15, X_{O_2}=0.126, Fr=0.5 and six different values of p. Left.- Propagation velocity evolution. Right.- Maximum propagation velocity.

P = 5%

P = 10%

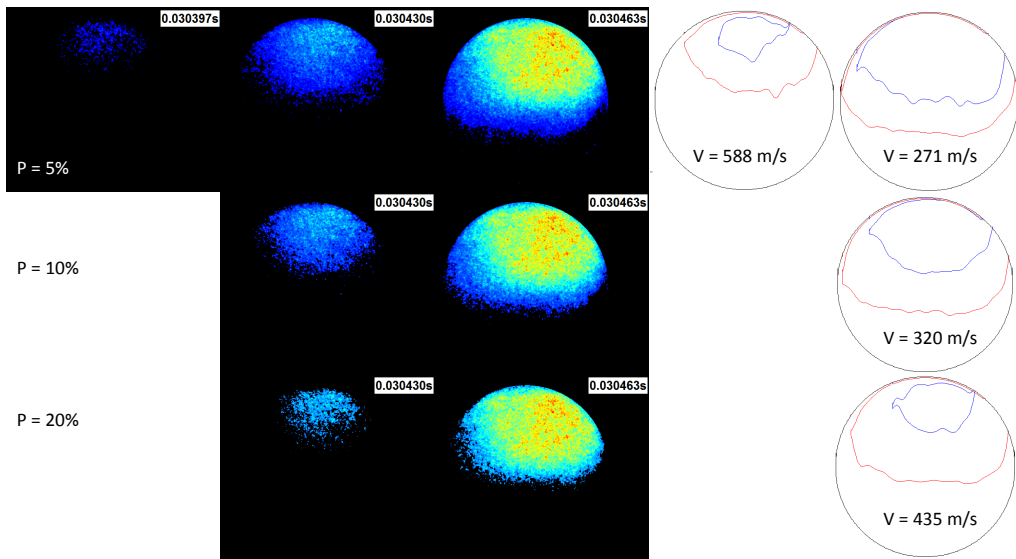P = 20%

V = 588 m/s   V = 271 m/s

V = 320 m/s

V = 435 m/s

Figure A.14: Processed images for the maximum propagation velocity shown in Fig. A.13. Three different p values are evaluated: 5%, 10% and 20%.

images with a different level of intensity are filtered using a too high p value, the lighted area will be further reduced in the darker image, resulting in a higher distance between perimeters and, consequently, in a higher propagation velocity. On the other hand, too low p values lead to a very smooth filtering, which can result in the existence of background noise in the images. The higher the radiation intensity, the higher the level of noise. Therefore, the filter threshold should depend on the difference between the maximum pixel intensity and the background noise intensity ($I_{max} - I_{back}$), as occurs with the one used in this investigation. However, too low p values lead to an insensitivity of the threshold to the maximum pixel intensity. Thus, images that had been previously considered as noise can be used for the evaluation of the propagation velocity, leading to unexpected results. This fact is described in Fig. A.14, in which the images that correspond to Fig. A.13 to the right are plotted for p values of 5%, 10% and 20%.

Values of p between 8% and 18% lead to approximately the same values of the propagation velocity. Specifically, $p = 10\%$ has been chosen in this study. It should be noted that p can take a constant value, since the effect of the maximum pixel intensity of each image is taken into account in the definition of the threshold. Therefore, despite the fact that a constant p value is used, the filter is based on the used dynamic range of each image.

Appendix B. Validity of τ correlations

Ignition delays from the Curran's detailed chemical kinetic mechanism for iso-octane and n-heptane have been parameterized using the Levenberg-Marquardt algorithm for minimizing the sum of the squares of the deviations.

The least-squares curve fitting results in the following expressions for iso-octane (Eq. B.1) and n-heptane (Eq. B.2), respectively:

$$\tau_{iso-oct} = 6.2697 \cdot 10^{-11} P^{-0.504} X_{O_2}^{-1.946} Fr^{-0.836} exp\left(\frac{14940}{T}\right) \qquad (B.1)$$

$$\tau_{n-hep} = 1.5931 \cdot 10^{-6} P^{-1.316} X_{O_2}^{-1.637} Fr^{-0.548} exp\left(\frac{8756}{T}\right) \qquad (B.2)$$

where the ignition delay, τ, is in seconds. P is the pressure in bar, Fr is the working equivalence ratio, X_{O_2} is the oxygen molar fraction and T is the temperature in K.

The following range of operating conditions was tested for the validation:

- Temperatures from 830 to 1400 K.

- Pressures from 40 to 165 bar.

- Equivalence ratios from 0.3 to 0.8.

- Oxygen molar fractions from 0.105 to 0.21.

Fig. B.15 shows the simulated ignition delays versus the ones obtained by means of Eqs. B.1 and B.2 for all the ignition points and both fuels. The line $y = x$, which represents a perfect match between values, has been also plotted in the figure. Finally, the Pearson's coefficient of correlation, R^2, has been calculated and its value has been added to the figure. It can be seen that the matching between simulations and correlations is pretty good in the range of thermodynamic conditions of interest.
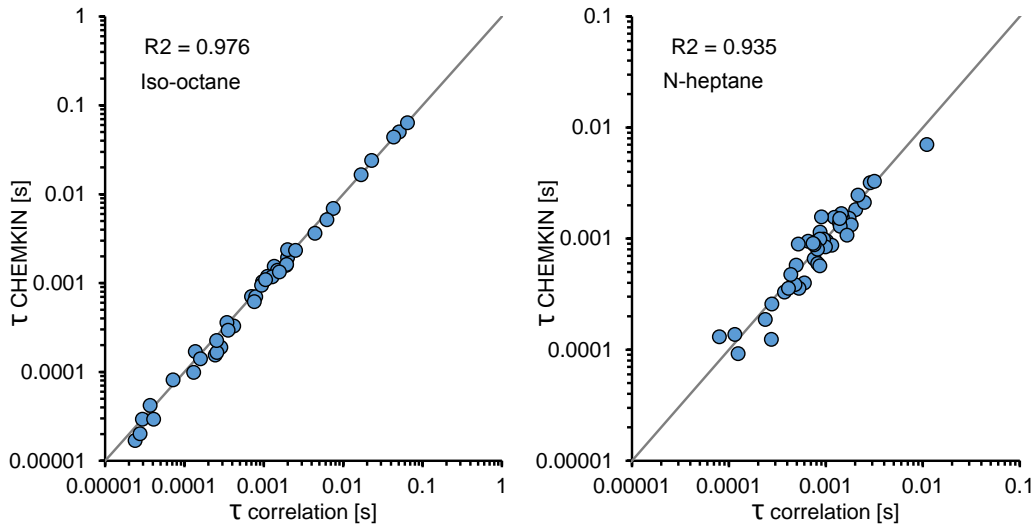
44

Figure B.15: Ignition delays from chemical simulations with CHEMKIN versus ignition delays from Eqs. 8 and 9

Appendix C. Estimation of the pressure wave intensity

The intensity of the incident pressure wave cannot be measured by the in-cylinder piezoelectric pressure sensor because it is located near the cylinder liner. Thus, a reflected wave is generated nearly at the same time that the incident wave reaches the sensor. Therefore, the maximum measured pressure wave is assumed to be an estimator of the pressure behind the reflected wave, and the intensity of the incident wave, which is indistinguishable because the reflected wave is generated just on the sensor, has to be estimated.

To do so, the following system of equations based on the Rankine-Hugoniot equations has to be solved:

$$\frac{P_r}{P_i} = \frac{2\gamma_i M_r^2 - (\gamma_i - 1)}{\gamma_i + 1} \tag{C.1}$$

45

$$\frac{P_i}{P_u} = \frac{2\gamma_u M_i^2 - (\gamma_u - 1)}{\gamma_u + 1} \tag{C.2}$$

$$\sqrt{1 + \frac{2(\gamma_i - 1)}{(\gamma_i + 1)^2}\left(\gamma_i M_i^2 - \frac{1}{M_i^2} - (\gamma_i - 1)\right)} = \frac{M_i - 1/M_i}{M_r - 1/M_r} \tag{C.3}$$

where the subscript u refers to the unburned mixture, i refers to the thermodynamic conditions behind the incident pressure wave and r refers to the thermodynamic conditions behind the reflected pressure wave. Besides, $M = u/a_u$ is the Mach number of the pressure wave, which relates the velocity of the wave to the speed of sound of the mixture in front of the wave (i.e., under the conditions of the unburned mixture). Thus, the Mach number of the incident wave, M_i, the Mach number of the reflected wave, M_r, and the pressure behind the incident wave, P_i, have to be calculated, while the pressure of the unburned mixture, P_u and the pressure behind the reflected wave, P_r, are measured by the piezoelectric sensor.

Finally, the temperature behind the incident pressure wave can be obtained as follows:

$$\frac{T_i}{T_u} = \frac{P_i}{P_u}\frac{(\gamma_u - 1)M_i^2 + 2}{(\gamma_u + 1)M_i^2} \tag{C.4}$$

References

[1] J. Lacey, K. Kameshwaran, Z. Filipi, W. Cannella, and P. Fuentes-Afflick. Influence of ethanol addition in refinery stream fuels and the HCCI combustion. *Fuel*, 126:122–133, 2014.

[2] G. Coskun, H.S. Soyhan, U. Demir, A. Turkcan, A.N. Ozsezen, and M. Canakci. Influences of second injection variations on combustion

and emissions of an HCCI-DI engine: Experiments and CFD modelling. *Fuel*, 136:287–294, 2014.

[3] B.-Q. He, J. Yuan, M.-B. Liu, and H. Zhao. Combustion and emission characteristics of a n-butanol HCCI engine. *Fuel*, 115:758–764, 2014.

[4] P. Das, P.M.V. Subbarao, and J.P. Subrahmanyam. Control of combustion process in an HCCI-DI combustion engine using dual injection strategy with EGR. *Fuel*, 159:580–589, 2015.

[5] Y. Liu, L. Li, J. Ye, J. Deng, and Z. Wu. Ion current signal and characteristics of ethanol/gasoline dual fuel HCCI combustion. *Fuel*, 166:42–50, 2016.

[6] L. Zhou and H. Wei. Chemistry acceleration with tabulated dynamic adaptive chemistry in a realistic engine with a primary reference fuel. *Fuel*, 171:186–194, 2016.

[7] H. Terashima and M. Koshi. Mechanisms of strong pressure wave generation in end-gas autoignition during knocking combustion. *Combustion and Flame*, 162:1944–1956, 2015.

[8] J. Dernotte, J. Dec, and C. Ji. Investigation of the sources of combustion noise in HCCI engines. *SAE Technical Paper*, 2014-01-1272, 2014.

[9] M. Sjoberg, J.E. Dec, and N.P. Cernansky. Potential of thermal stratification and combustion retard for reducing pressure-rise rates in HCCI engines, based on multi-zone modeling and experiments. *SAE Technical Paper*, 2005-01-0113, 2005.

670 [10] D. Bradley, C. Morley, X.J. Gu, and D.R. Emerson. Amplified pressure waves during autoignition: Relevance to CAI engines. *SAE Technical Paper*, 2002-01-2868, 2002.

673 [11] X.J. Gu, D.R. Emerson, and D. Bradley. Modes of reaction front propagation from hot spots. *Combustion and Flame*, 133:63–74, 2003.

675 [12] J.H. Chen, E.R. Hawkes, R. Sankaran, S.D. Mason, and H.G. Im. Direct numerical simulation of ignition front propagation in a constant volume with temperature inhomogeneities I. fundamental analysis and diagnostics. *Combustion and Flame*, 145:128–144, 2006.

679 [13] C.S. Yoo, T. Lu, J.H. Chen, and C.K. Law. Direct numerical simulations of ignition of a lean n-heptane/air mixture with temperature inhomogeneities at constant volume: Parametric study. *Combustion and Flame*, 158:1727–1741, 2011.

683 [14] G. Bansal and H.G. Im. Autoignition and front propagation in low temperature combustion engine environments. *Combustion and Flame*, 158:2105–2112, 2011.

686 [15] R. Augusta, D.E. Foster, J.B. Ghandhi, J. Eng, and P.M. Najt. Chemiluminescence measurements of homogeneous charge compression ignition (HCCI) combustion. In SAE Technical Papers, editor, *2006 SAE World Congress*, Detroit, MI; United States, 3 2006. Code 90162.

690 [16] H.F. Liu, M.F. Yao, C. Jin, P. Zhang, Z.M. Li, and Z.Q. Zheng. Chemiluminescence spectroscopic analysis of homogeneous charge compres-

sion ignition combustion processes. *Spectroscopy and Spectral Analysis*, 30:2611–2615, 2010.

[17] A. Dubreuil, F. Foucher, and C. Mounaim-Rousselle. Analysis of flame and OH* natural emissions of n-heptane combustion in a Homogeneous Charge Compression Ignition (HCCI) engine: Effect of burnt gas dilution. *Energy and Fuels*, 23:1406–1411, 2009.

[18] H.F. Liu, Z. Zheng, M. Yao, P. Zhang, Z. Zheng, B. He, and Y. Qi. Influence of temperature and mixture stratification on HCCI combustion using chemiluminescence images and CFD analysis. *Applied Thermal Engineering*, 33:135–143, 2012.

[19] J. M. Desantes, J.M. Garcia-Oliver, W. Vera-Tudela, D. López-Pintor, B. Schneider, and K. Boulouchos. Study of the auto-ignition phenomenon of PRFs under HCCI conditions in a RCEM by means of spectroscopy. *Applied Energy*, 179:389–400, 2016.

[20] J. M. Desantes, J.M. Garcia-Oliver, W. Vera-Tudela, D. López-Pintor, B. Schneider, and K. Boulouchos. Study of ignition delay time and generalization of auto-ignition for PRFs in a RCEM by means of natural chemiluminescence. *Energy Conversion and Management*, 111:217–228, 2016.

[21] J. M. Desantes, J. J. López, S. Molina, and D. López-Pintor. Design of synthetic EGR and simulation study of the effect of simplified formulations on the ignition delay of isooctane and n-heptane. *Energy Conversion and Management*, 96:521–531, 2015.

49

[22] G. Woschni. A universally applicable equation for the instantaneous heat transfer coefficient in the internal combustion engine. *SAE Paper no. 670931*, 1967.

[23] J. Benajes, P. Olmeda, J. Martin, and R. Carreño. A new methodology for uncertainties characterization in combustion diagnosis and thermodynamic modelling. *Applied Thermal Engineering*, 71:389–399, 2014.

[24] F. Payri, S. Molina, J. Martin, and O. Armas. Influence of measurement errors and estimated parameters on combustion diagnosis. *Applied Thermal Engineering*, 26:226–236, 2006.

[25] A.G. Gaydon. *The Spectroscopy of Flames.* Chapman and Hall, 1974.

[26] J.M. Desantes, J.J. López, J.M. Garcia-Oliver, and D. López-Pintor. A 5-zone model to improve the diagnosis capabilities of a Rapid Compression-Expansion Machine (RCEM) in autoignition studies. *SAE World Congress*, 2017-01-0730, 2017.

[27] J.M. Desantes, J. Arregle, S. Molina, and M. Lejeune. Influence of the EGR rate, oxygen concentration and equivalent fuel/air ratio on the combustion behavior and pollutant emissions of a heavy-duty diesel engine. *SAE Technical Paper*, 2000-01-1813, 2000.

[28] J.B. Heywood. *Internal combustion engine fundamentals.* Mc Graw Hill, 1988.

[29] M. Metghalchi and J.C. Keck. Burning velocities of mixtures of air with methanol, isooctane, and indolene at high pressure and temperature. *Combustion and Flame*, 48:191–210, 1982.

[30] Y.B. Zeldovich. Regime classification of an exothermic reaction with nonuniform initial conditions. *Combustion and Flame*, 39:211–214, 1980.

[31] H. J. Curran, P. Gaffuri, W. J. Pitz, and Charles K. Westbrook. A comprehensive modeling study of n-heptane oxidation. *Combustion and Flame*, 1997.

[32] H. J. Curran, P. Gaffuri, W. J. Pitz, and C. K. Westbrook. A comprehensive modeling study of iso-octane oxidation. *Combustion and Flame*, 129:253–280, 2002.

[33] J. M. Desantes, V. Bermudez, J. J. López, and D. López-Pintor. A new method to predict high and low-temperature ignition delays under transient thermodynamic conditions and its experimental validation using a Rapid Compression-Expansion Machine. *Energy Conversion and Management*, 123:512–522, 2016.

[34] José M. Desantes, Vicente Bermúdez, J. Javier López, and Darío López-Pintor. Experimental validation of an alternative method to predict high and low-temperature ignition delays under transient thermodynamic conditions for PRF mixtures using a Rapid Compression-Expansion Machine. *Energy Conversion and Management*, 129:23–33, 2016.

[35] N Semenov. Nacatm 1026 (1942) trans, from prog. *Phys. Sci.(USSR) Vol*, 24:433, 1940.